CORONAVIRUS

Intermediates in SARS-CoV-2 spike–mediated cell entry

Tara C. Marcink[1,2], Thomas Kicmal[3], Emily Armbruster[4], Zhening Zhang[5], Gillian Zipursky[1,2], Kate L. Golub[1,2], Mohab Idris[1,2], Jonathan Khao[6], Jennifer Drew-Bear[1,2], Gael McGill[6,7], Tom Gallagher[3]*, Matteo Porotto[1,2,8]*, Amédée des Georges[4,9,10]*, Anne Moscona[1,2,11,12]*

SARS-CoV-2 cell entry is completed after viral spike (S) protein–mediated membrane fusion between viral and host cell membranes. Stable prefusion and postfusion S structures have been resolved by cryo–electron microscopy and cryo–electron tomography, but the refolding intermediates on the fusion pathway are transient and have not been examined. We used an antiviral lipopeptide entry inhibitor to arrest S protein refolding and thereby capture intermediates as S proteins interact with hACE2 and fusion-activating proteases on cell-derived target membranes. Cryo–electron tomography imaged both extended and partially folded intermediate states of S2, as well as a novel late-stage conformation on the pathway to membrane fusion. The intermediates now identified in this dynamic S protein–directed fusion provide mechanistic insights that may guide the design of CoV entry inhibitors.

INTRODUCTION

Infection by SARS- CoV-2 is mediated by the viral surface spike (S) glycoprotein and requires fusion between the viral and host cell membranes. S is a 1273-residue heavily glycosylated type I integral membrane protein that exists as a trimer on the virion surface and mediates attachment, receptor binding, and membrane fusion. Proteolytic cleavage of S by host proteases generates peripheral S1 and integral membrane S2 fragments (*1*). Upon S1 binding to a host cell membrane angiotensin-converting enzyme 2 (hACE2) and subsequent secondary proteolytic cleavage at S2′ (*2*), S2 undergoes large structural transitions from prefusion conformations to transient extended intermediates that insert into the target host membrane. Refolding of extended S2 intermediates through a "zippering" of the C-terminal heptad repeat region (HRC/HR2) onto the N-terminal heptad repeat region (HRN/HR1) pulls the viral and host membranes together to initiate fusion and delivery of the viral genome into the host cell. The final refolded S2′ is a stable six-helix bundle (*3*, *4*). Antiviral fusion inhibitory peptides corresponding to the HRC domain interfere with the structural transitions and inhibit fusion (*3*, *5*, *6*), serving as valuable tools for structural analysis of intermediate steps in S-mediated viral entry. The lipid-conjugated $[SARS_{HRC}\text{-}PEG_4]_2$-chol forms a heterologous six-helix bundle by associating with the HRN domains of S2, blocks viral entry, and prevents direct-contact transmission of SARS-CoV-2 in ferrets (*3*, *5*).

The S-hACE2 interfaces and the prefusion and postfusion S structures have been resolved by x-ray crystallography (*7*, *8*), cryo–electron microscopy (cryo-EM) (*9*–*11*), and cryo–electron tomography (cryo-ET) (*12*–*14*), but the intermediate states of S2 remain elusive. The intermediate states of class I fusion proteins are transient and unstable, and only recently has it been possible to view intermediates of HIV-1 gp41, parainfluenza virus type 5 (PIV5) F, and influenza hemagglutinin (HA2) (*15*–*17*). We recently characterized the intermediates of the human parainfluenza virus type 3 (HPIV3) fusion complex using cryo-ET (*18*). Here, we dissect the intermediates of SARS-CoV-2 fusion including the prefusion S bound to hACE2 and the extended and partially folded intermediate states of S2. The antiviral $[SARS_{HRC}\text{-}PEG_4]_2$-chol lipopeptide stalls the refolding of the S2 intermediate to reveal a novel late-stage S protein conformation on the pathway to membrane fusion, decoupling the formation of the partially folded intermediate state from subsequent membrane merger and viral fusion.

RESULTS

Virus-like particles and target extracellular vesicles as surrogates for authentic virions and cells

To characterize sequential structural transitions in SARS-CoV-2 spike proteins, we used cryo-ET to image interactions between corona virus-like particles (VLPs) and target extracellular vesicles (tEVs) (*19*). The VLPs reflect authentic virions and include S, envelope (E), membrane (M), and nucleocapsid (N) proteins (Fig. 1Aia) as confirmed by Western blot (fig. S1A). The N proteins within particle interiors are appended with nanoluciferase fragment (HiBiT) tags. The tEVs contain human hACE2 linked to intravesicular complementary nanoluciferase (LgBiT) fragments (Fig. 1Aib). The VLPs and tEVs were purified using size exclusion columns (fig. S1, B and C), which preserved native S protein conformations. Mixtures of purified VLPs and tEVs were exposed to trypsin (Fig. 1B), a serine protease that can replace TMPRSS2 in cleaving at the S2′ site to activate membrane fusion (*2*). The S-directed VLP-tEV fusions (Fig. 1Aiv) were quantified by HiBiT:LgBiT complementation into nanoluciferase, measured by luminometry (Fig. 1C and fig. S2, A and B) (*2*). With mixtures of purified VLPs and tEVs, we observed a dose-dependent luminescence curve with increasing amounts of trypsin. There was no fusion with the lowest concentrations of

[1]Department of Pediatrics, Columbia University Vagelos College of Physicians and Surgeons, New York, NY, USA. [2]Center for Host-Pathogen Interaction, Columbia University Vagelos College of Physicians and Surgeons, New York, NY, USA. [3]Department of Microbiology and Immunology, Loyola University Chicago, Maywood, IL, USA. [4]Structural Biology Initiative, CUNY Advanced Science Research Center, City University of New York, New York, NY, USA. [5]Department of Biochemistry and Molecular Biophysics, Columbia University Vagelos College of Physicians and Surgeons, New York, NY, USA. [6]Digizyme Inc., Brookline, MA, USA. [7]Center for Molecular and Cellular Dynamics, Department of Biological Chemistry and Molecular Pharmacology, Harvard Medical School, Boston, MA, USA. [8]Department of Experimental Medicine, University of Campania "Luigi Vanvitelli," 81100 Caserta, Italy. [9]Department of Chemistry and Biochemistry, The City College of New York, New York, NY, USA. [10]Ph.D. Programs in Chemistry and Biochemistry, The Graduate Center, City University of New York, New York, NY, USA. [11]Department of Microbiology and Immunology, Columbia University Vagelos College of Physicians and Surgeons, New York, NY, USA. [12]Department of Physiology and Cellular Biophysics, Columbia University Vagelos College of Physicians and Surgeons, New York, NY, USA.
*Corresponding author. Email: tgallag@luc.edu (T.G.); adesgeorges@gc.cuny.edu (A.d.G.); mp3509@cumc.columbia.edu (M.P.); am939@cumc.columbia.edu (A.M.)

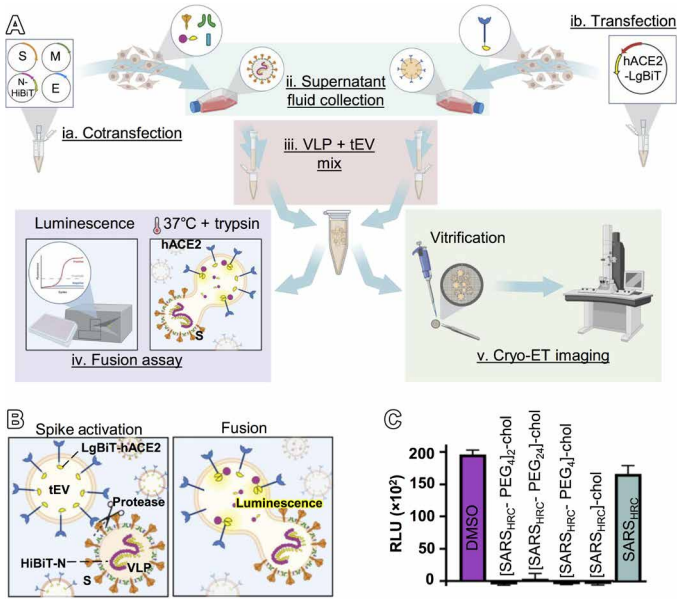

Fig. 1. VLP and tEV as surrogates for SARS-CoV-2 virus-cell fusion. (**A**) (ia) Plasmids encoding the SARS-CoV-2 spike (S), envelope (E), membrane (M), and N-terminal HiBiT-tagged nucleoprotein (HiBiT-N) were cotransfected, and (ib) plasmids encoding hACE2 were separately transfected into HEK293T cells. (ii) Supernatant fluids were harvested after 2 days. VLPs and tEVs were purified by size exclusion chromatography (SEC). (iii) Purified VLPs and tEVs were mixed and used for (iv) fusion assays and (v) cryo-ET. (**B**) Schematic of spike activation using exogenous protease with resultant fusion measured by complementation between tEV LgBiT and VLP HiBiT from the VLP (fluorescent yellow). (**C**) Monomeric and dimeric SARS-CoV-2 inhibitory peptides were assessed in viral fusion assays using VLPs and tEVs. Relative luminescence units (RLU) were plotted 30 min after the temperature was raised to 37°C.

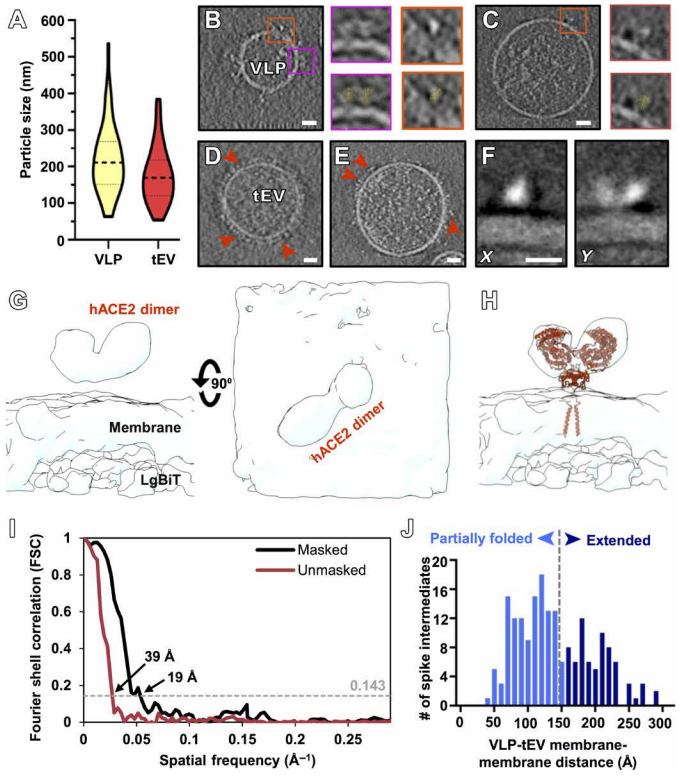

Fig. 2. Visualization of VLPs and tEVs by cryo-electron tomography. (**A**) VLPs (yellow) and tEVs (red) show particle sizes ranging from 50 to 500 nm with a mean of 200 nm for VLPs ($n = 50$) and 175 nm for tEVs ($n = 50$). (**B** and **C**) Contrast-inverted tomogram slice of two different-sized VLPs. Insets show prefusion spikes without (top insets) and with (bottom insets) prefusion spike atomic model (PDB ID: 5x58) fit into the raw tomogram densities. (**D** and **E**) Contrast-inverted tomogram slices of tEVs at 4°C (D) and 37°C (E) with densities attributable to hACE2 on the surface of tEVs (red arrowheads). (**F**) *X* and *Y* projections from the final subtomogram reconstruction of hACE2. (**G** and **H**) Side view and top view without (G) and with (H) hACE2 model (PDB ID: 6M1D) (*11*) fit into the subtomogram averaged density map. (**I**) Fourier shell correlation (FSC) plots of the hACE2 density map with and without a mask. (**J**) Distribution of VLP membrane to tEV membrane distance measurements where spike intermediates were identified. Intermediate spikes whose VLP membrane to tEV membrane distance measured less than 15 nm ($n = 116$) were in a partially refolded state, while above 15 nm ($n = 76$), these spikes were in an extended state. Spike intermediates range from 3 to 29 nm ($n = 192$). Scale bars, (B to E) 10 nm and (F) 5 nm.

trypsin (fig. S2C). There was also no fusion when VLPs lacked S proteins or when tEVs lacked hACE2 (fig. S2). These quantitative assays confirm that prefusion S and functional hACE2 proteins are present on VLPs and tEVs, and they establish correlations between "bulk" population-wide fusion and images of individual postfusion vesicles observed in cryo–electron tomograms (Fig. 1A, iv and v).

To arrest fusion and image the stalled S protein intermediates, we introduced a panel of fusion inhibitory peptides that bind to the activated S2 protein and prevent the progression to fusion (*3*, *5*). When these peptides were present during VLP-tEV coincubation, we observed complete suppression of fusion (Fig. 1C). Results were similar to those obtained with authentic virus (*5*). We chose the dimeric [SARS$_{HRC}$-PEG$_4$]$_2$-chol lipopeptide for use in imaging experiments because of its superior potency and robust inhibition of fusion mediated by the S proteins of several emergent SARS-CoV-2 variants (*5*).

Characteristics of VLPs and tEVs identified with cryo-ET at 4° and 37°C

The VLPs and tEVs range in diameter from 50 to 500 nm (Fig. 2A); both contain cellular material, while some of the VLPs contained long nucleoprotein strands (Fig. 2, B and C). Prefusion S protein conformations extending from VLP surfaces were distributed more sparsely than observed on infectious virions (Fig. 2, B and C) (*20*). hACE2 distribution on the tEVs ranged from densely to sparsely packed (Fig. 2, D and E). VLPs were distinguishable from tEVs by their characteristic tree-like spike proteins; tEVs, in contrast, display dimeric hACE2 with a discrete "Y" shape. To confirm the tEVs that were incubated with VLPs contained hACE2, we performed subtomogram averaging of the densities at the surface of tEVs. The density of the 19-Å-resolution subtomogram corresponds to the size and shape of dimeric hACE2 (Fig. 2, F to I), and the atomic model of full-length ACE2 [Protein Data Bank (PDB) ID: 6M1D] (*11*) fits well into it (Fig. 1H).

When VLPs and tEVs were coincubated at 37°C for 30 min with trypsin, fusion was detected by luminometry (Fig. 1C and fig. S2). Using the trypsin-incubated samples for cryo-ET, we captured and imaged fully fused particles where S and hACE2 were present on the same membrane surfaces (fig. S3). The shapes of the fused particles

were elongated with membrane perturbations, similar to tomographic images of HPIV3 (*18*) and influenza (*16*).

We then incubated VLPs and tEVs on cryo-ET grids at 37°C in the presence of the $[SARS_{HRC}\text{-}PEG_4]_2$-chol lipopeptide inhibitor before vitrification. Under these conditions, we never observed any images where S and hACE2 were present on continuous membranes, consistent with the bulk population-based measurements of VLP-tEV fusion. Instead, the resulting tomograms revealed a suite of densities that correspond to different states of the S protein in areas of interaction between VLP and tEV (n = 192) (Fig. 2J and fig. S4). All S proteins distant from the VLP-tEV interaction site were found in a postfusion conformation with a distinct elongated tree-like structure (fig. S5). Subtomogram averaging of the tEV surface proteins in the presence of VLPs showed the dimeric hACE2 in the discrete Y shape with a resolution of 19 Å (Fig. 2, F to I). Characterization of these two distinct features allowed for identification of paired vesicles.

Interactions between hACE2 and the prefusion spike

Prefusion spike proteins on VLPs were captured during interaction with hACE2 on tEVs, after incubation at 37°C in the presence of the inhibitory peptide. About 8% of the tomograms (n = 12) showed densities corresponding to the prefusion spikes bound to hACE2 in regions where VLP and tEV membranes were far apart (>20 nm). The length of the continuous density spanning VLP and tEV membranes, comprising hACE2 and prefusion spike in sequence, was 25 to 30 nm. Our model of those interactions is shown as a schematic derived from a coarse-grained molecular mechanics (CG-MM) simulation guided by the tomographic densities (Fig. 3A) using a method refined from (*5*). In some cases, multiple spikes appeared bound to multiple hACE2 molecules (Fig. 3, B to M). We fitted models of the hACE2 dimer cryo-EM structure with the S1 receptor binding domains (RBDs) attached (PDB ID: 7L7F) (*21*) and the prefusion spike cryo-EM structure (PDB ID: 6X2B) (*22*) into these tomogram densities. We identified densities consistent with prefusion spikes bound to hACE2 (Fig. 3, F to M) with either one (Fig. 3, F and G), two (Fig. 3, H to J), or three (Fig. 3, B to E, and movie S1) hACE2 molecules bound to a single spike protein. Variability was evident in the hinge region of these prefusion spikes, with different degrees of bending (Fig. 3G compared to Fig. 3L). When the samples were incubated at 4°C, we only observed prefusion spike proteins interacting with hACE2, without progression to subsequent transitional stages (fig. S6).

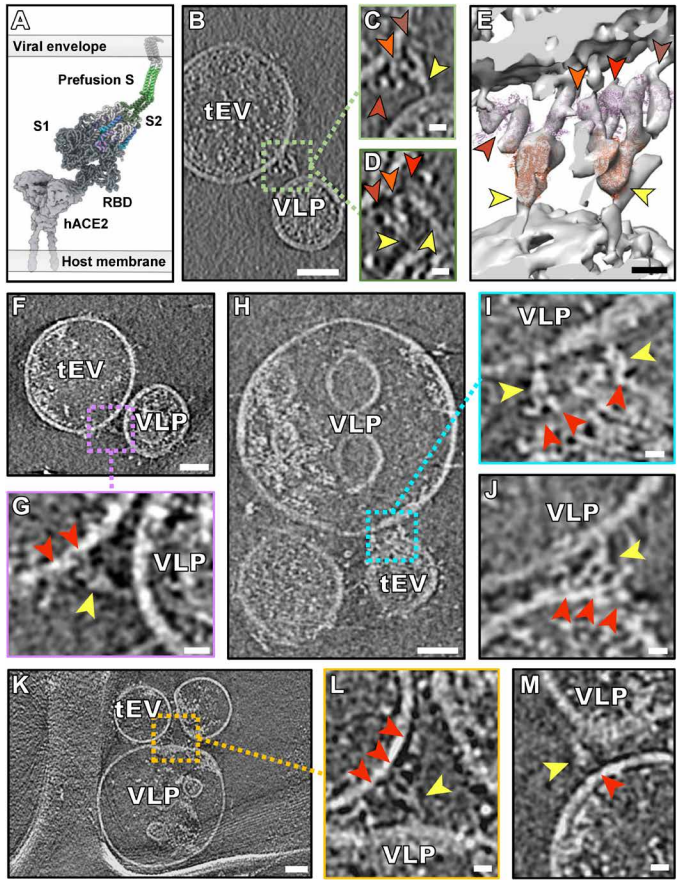

Fig. 3. Interaction between hACE2 and prefusion spike. (**A**) Schematic derived from a coarse-grained molecular mechanics (CG-MM) simulation guided by the tomographic densities of prefusion spike (S1 + S2) bound to hACE2. (**B**, **F**, **H**, and **K**) Contrast-inverted slices through tomograms of VLPs containing spike and tEVs containing hACE2. (**C**, **D**, **G**, **I**, **J**, **L**, and **M**) Enlarged views of tomograms with densities attributed to S (yellow arrows) interacting with densities attributed to hACE2 (shades of red arrowheads). (**E**) Isosurface representation of a tomogram from (B) to (D) with densities attributed to four hACE2 dimers [shades of red arrowheads corresponding to arrowheads in (C) and (D)] and two S proteins with their RBDs oriented upward (yellow arrowhead). Ribbon models fitted into the density map are displayed in purple for hACE2 (PDB ID: 7L7F) and orange for S (PDB ID: 6X2B). Full set of tomogram *z* slices and the isosurface representation are displayed as movie S1 for (B) to (E). Scale bars, (B, F, H, and K) 50 nm and (C to E, G, I, J, L, and M) 10 nm.

The transient extended intermediate state of the spike protein

In regions where membranes were closer to each other but more than 15 nm apart, we observed extended spike intermediates (Fig. 4 and fig. S4, A and B). A model of these interactions is shown as a schematic derived from a CG-MM simulation guided by the tomographic densities (Fig. 4A). These extended intermediate spikes were captured in the experimental conditions of VLPs and tEVs incubated with $[SARS_{HRC}\text{-}PEG_4]_2$-chol lipopeptide at 37°C and appeared in multiple regions where the tEV and VLP membranes were in close proximity but not in contact (Fig. 4, B to E, and movies S2 and S3). Plot profiles of the S diameter averaged 3.1 nm wide (n = 22) (Fig. 4, F and G) and were similar to other viral fusion protein intermediates measured by cryo-ET, including those of HPIV3 (*18*) and PIV5 (*15*). The S intermediates present multiple configurations and angles with respect to the membranes, as might be expected indicating that the $[SARS_{HRC}]_2\text{-}PEG_{11}$ (dimeric peptide without lipid) or $[SARS_{HRC}\text{-}PEG_4]_2$-chol peptides do not restrict the conformational spectrum of these extended S intermediates. This finding contrasts with the consistent conformations observed for HPIV3 fusion protein (F) (*18*). For HPIV3, the receptor binding protein is a separate protein that remains in association with F during the fusion process and thereby stabilizes the intermediate states, but for SARS-CoV-2 S, it appears that after release of S1, the S2 portion has greater flexibility during the sequential transition states (*12*, *20*). The orientation adopted by S2 varies in part with the distance between VLP and tEV membranes (Fig. 4, H to J), which ranges between 25 nm on the wider outer edge of the interface and 5 nm near the center of these membrane-membrane interfaces. This implies that the peptides do not restrict flexibility at S protein "hinges" (*20*).

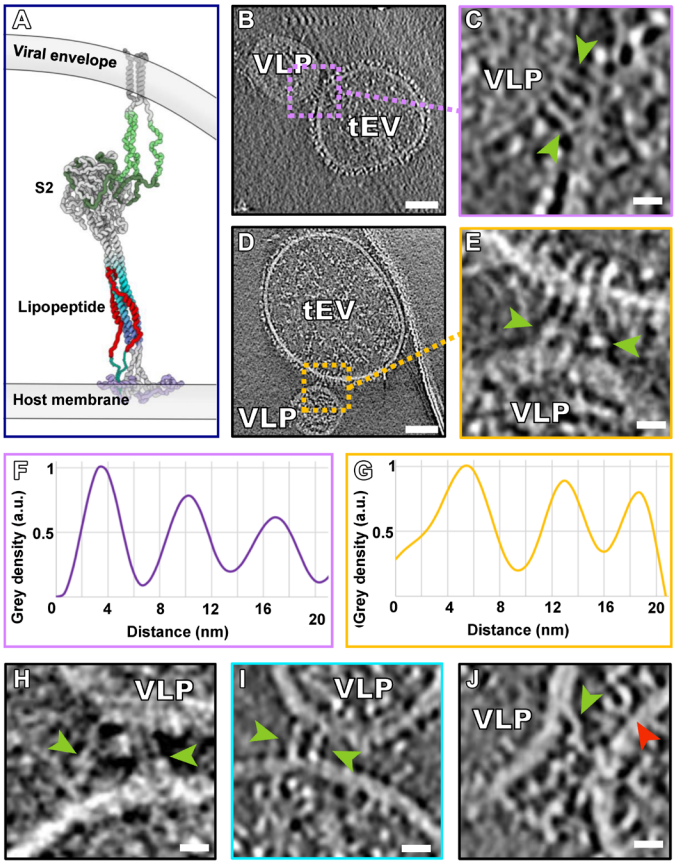

Fig. 4. Extended intermediate state of the spike protein. (**A**) Schematic derived from a CG-MM simulation guided by the tomographic densities of extended intermediate states of S2. (**B** and **D**) Contrast-inverted slices from tomograms of VLPs bearing S and tEVs bearing hACE2 showing densities (green arrowheads) that appear to be spikes in their extended state. (**C** and **E**) Enlarged views of tomograms showing densities (green arrowheads) attributed to S proteins in an extended state. (**F** and **G**) Distance plot of S intermediates measured between the green arrows of (B) and (D), respectively. a.u., arbitrary units. (**H** to **J**) Additional enlarged views from tomogram slices showing extended intermediate S (green arrowheads) spanning VLP and tEV membranes. Densities matching hACE2 are found in close proximity to the region of S insertion (red arrowheads). Scale bars, (B and D) 50 nm and (C, E, and H to J) 10 nm.

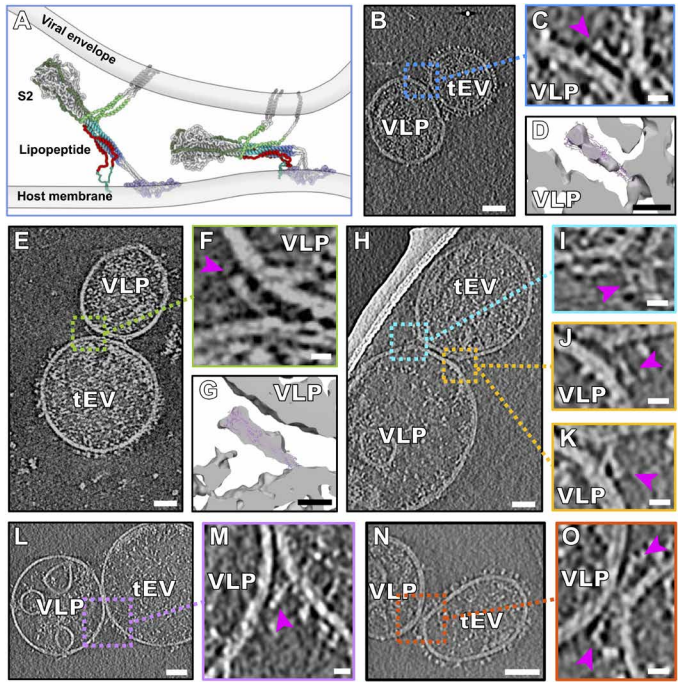

Fig. 5. Partially folded intermediate state of the spike protein. (**A**) Schematic derived from a CG-MM simulation guided by the tomographic densities of partially folded intermediate states of S2 spanning the viral and host membranes. (**B**, **E**, **H**, **L**, and **N**) Contrast-inverted slices from tomograms of VLPs bearing S and tEVs bearing hACE2, showing densities attributable to the partially folded intermediate state of S. (**C**, **F**, **I** to **K**, **M**, and **O**) Enlarged regions from tomogram slices showing densities attributable to S partially folded intermediates (purple arrowheads) linking VLP and tEV membranes. (**D** and **G**) Isosurface representations of (C) and (F) with the postfusion S (PDB ID: 6M3W) fitted into the map density. Movie from *z* slices of tomogram displayed in (K) and (M) is shown as movies S2 and S3, respectively. Scale bars, (B, E, H, L, and N) 50 nm and (C, D, F, G, I to K, M, and O) 10 nm.

The partially folded intermediate states of the spike proteins

In the central regions of interaction where VLPs and tEVs were found in tight contact, the membranes were <15 nm apart (Fig. 5 and fig. S4, C and D). A schematic model of these interactions was derived from a CG-MM simulation guided by these tomographic densities (Fig. 5A). These regions of tight interaction spanned large sections of the VLP and tEV, with some densities similar to the postfusion S2 cryo-EM structure (Fig. 2, B to G) alongside densities that show sharp bending of the membrane at either edge (Fig. 5H). We fitted models of the published postfusion S2 cryo-EM structure (PDB ID: 6M3W) (*23*) into the cryo-ET densities, confirming that these densities are of the size and shape of postfusion S (Fig. 5, D and G). We identified multiple conformations of such partially folded intermediates of S at the edges of VLP-tEV interaction areas (Fig. 5, H to O, and fig. S4). In the presence of an inhibitory peptide without the cholesterol moiety that anchors the peptide in membranes ($[SARS_{HRC}]_2$-PEG_{11}), we also saw the full range of folded intermediate states (fig. S7), confirming that the peptide (and not the lipid moiety) prevented fusion and arrested S2 in a partially folded conformation.

Despite many examples of the partially folded S configuration (Fig. 5, movies S2 and S3, and fig. S4), we did not observe hemifusion or fused particles in the presence of the peptide in any of our tomograms (n = 153). While this configuration closely resembles the postfusion conformation and accommodates the postfusion S structure into its cryo-ET density, the S is attached to the two opposed membranes. Our working model for this process is that the peptide inhibitors permit progression to the partially folded intermediate state that just precedes fusion, preventing only the final complete zippering of the membrane-proximal ends. Thus, formation of the partially folded intermediate does not appear sufficient to drive fusion, as had been suggested for influenza HA and proposed as a general mechanism for class I and II viral fusion proteins (*24*), because the S attains an advanced refolded but not fully zippered state. Membrane fusion may require zippering of the membrane-proximal ends to bring the opposing membranes toward each other closer than what is observed here (*24*). In the *xy* plane of 14% of the tomograms (n = 21), we observe the partially folded intermediate spike proteins in close proximity and opposing each

other on either sides of point of interaction between VLP and tEV, representing the penultimate step of uninhibited pore formation (Fig. 5, N and O). We also visualized these partially folded intermediates on either side of the VLP-tEV membranes in the less-defined *z* direction of the tomograms (fig. S8). The inhibitory peptide blocks six-helix bundle formation by the HRC and HRN domains of S2; however, the S2 partially folded intermediates resemble the partially folded intermediates of influenza HA that have been observed at fusion pores (*25*). On surfaces of the VLPs that were distant from the VLP-tEV interaction sites, only late needle-like refolded spike structures were observed (fig. S5 and movies S2 and S3), indicative of unproductive proteolytic activation and transition to postfusion states.

Taking these images together, it is possible to reconstruct the sequence of events starting with spike protein binding, S2 activation to an extended state, S1 release, and subsequent refolding to a partially folded intermediate state where only the most membrane-proximal ends remain unzippered in the presence of inhibitory peptide (Fig. 6).

DISCUSSION

The use of luciferase "BiT" reporter-tagged SARS-CoV-2 VLPs and ACE2 tEVs allowed us to relate population-wide measurements of VLP-tEV fusion with the individual S-mediated vesicle fusions inferred by cryo-ET imaging. The "total" population-based measurements registered an average of complete VLP-tEV fusion and its inhibition by antiviral peptides. Using cryo-ET, variable fusion intermediate states were evident among heterogeneous vesicles, which brought out insights on S protein refolding during membrane fusion. We suggest that these intermediate states, now visualized by cryo-ET, reflect those present transiently during authentic SARS-CoV-2 cell entry.

Cryo-ET microscopy necessarily reveals very small subsets of the total vesicle populations. That the selected images presented in this report depict biologically meaningful S:ACE2-directed membrane fusion processes is apparent based on several features. First, VLP-tEV fusions as measured by the luciferase complementation assays were entirely dependent on VLP S proteins, tEV ACE2 proteins, and fusion-activating trypsin (fig. S2A). Second, without trypsin, complexed vesicles were not observed in any cryo–electron tomograms (Fig. 2, B and C). Yet with trypsin, complexed vesicles containing postfusion S and dimeric ACE2 were routinely observed (fig. S5). Third, the S and ACE2 proteins were evident on the same continuous membranes (fig. S3).

Notably, in relation to authentic SARS-CoV-2 virions, the S proteins were inefficiently incorporated into VLPs (*12*, *26*). Although sparse, the S proteins were evident, as were the central CoV structural proteins E, M, and N (fig. S1A). VLPs contained prefusion S proteins (Fig. 2, B and C) that were functionally active (fig. S2) and converted to postfusion forms upon exposure to trypsin (fig. S5). Cooperative juxtapositioning of few or several viral fusion proteins is a known prerequisite for complete membrane coalescence (*27*). It is therefore conceivable that some VLP-tEV interactions do not culminate in fusion, even in the absence of inhibitory peptides.

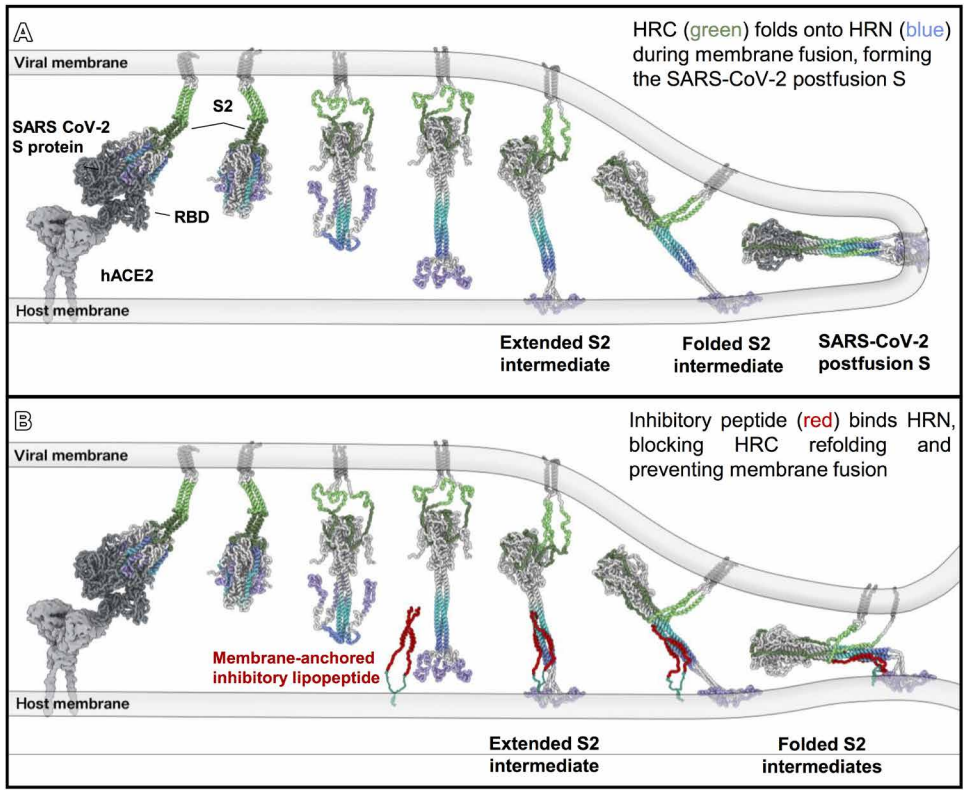

Fig. 6. Proposed model of fusion inhibition by [$SARS_{HRC}$-PEG_4]$_2$-chol. (**A**) Model of interaction between SARS-CoV-2 prefusion S on the viral envelope and hACE2 on the host cell membrane. After detachment of S1, S2 unfolds and inserts into the host membrane. Refolding of S2 to a postfusion state leads to membrane fusion. (**B**) Model of antiviral lipopeptide mechanism with the lipopeptide anchored into the host membrane and binding the HRN region of S2, perturbing the final conformational changes of S2 intermediates and preventing membrane fusion.

With peptides present, fusion is halted, irrespective of presumed variable S protein densities on VLPs.

Fusion inhibitory peptides that bind the HRN domain of S2 and stall progression to end-stage S protein conformations (*3*, *5*) were central in our analyses and suppressed average fusion signals to background levels (Fig. 1C). Several states that were not previously observed were evident under these experimental conditions, including the complete prefusion S with S1 bound to hACE2 (Fig. 3), the extended intermediate state of S2 (Fig. 4), and the partially folded, near end-stage, intermediate state in the presence of fusion inhibitory peptide (Fig. 5). While the transient extended state was not observed only in its putative fully extended conformation, it was examined in a series of refolding steps before attaining the partially folded state. In the presence of peptide, formation of the partially folded form of S2 is not sufficient to drive fusion; our model is that the membrane-proximal ends fail to unite and fusion does not occur. A recent report (*28*) describes a broadly neutralizing monoclonal anti-S antibody shown by cryo-EM and crystal structure to bind the stem helix of prefusion S; the antibody inhibits membrane fusion, and the proposed neutralization mechanism is prevention of S2 subunit refolding from the prefusion to the postfusion state. The intermediate states in the fusion process shown in our study (Figs. 3 to 5) and the implied functional models revealed by imaging the transient intermediates during the refolding steps (Fig. 6) should advance the framework for mechanistic approaches to interfering with viral entry.

MATERIALS AND METHODS

Production and isolation of VLPs

Human embryonic kidney (HEK) 293T cells were seeded in 145-cm^2 tissue culture plates and grown in 10% fetal bovine serum–Dulbecco's modified Eagle's medium (DMEM) to 80 to 90% confluency. The cells were then cotransfected with SARS-CoV-2 S/D614G, M, E, and HiBiT-N encoding plasmids (16 μg total, 4 μg each) using LipoD293 (SignaGen) reagent 3:1 LipoD293 (microliters):plasmid (micrograms). S/D614G plasmid was replaced with empty vector (pcDNA3.1) to produce spikeless VLPs. At 16 hours posttransfection (p.t.), media were changed to serum-free DMEM (SFM), and then at 48 hours p.t., media were harvested and clarified by differential centrifugation (300*g* for 10 min at 4°C and then 3000*g* for 10 min at 4°C). Clarified media were concentrated >40-fold using Amicon Ultra-15 100-K ultrafilters. Concentrated VLPs were further purified by size exclusion chromatography (SEC), using qEVoriginal 35-nm SEC columns (IZON). VLPs were eluted from columns using phosphate-buffered saline (PBS) (pH 7.4). To detect eluted VLPs, 5-μl aliquots of 500-μl fractions were mixed with 35 μl of passive lysis buffer (Promega) containing LgBiT and Nano-Glo substrate (Promega); relative luminescence units (RLU) were then measured in a plate-read luminometer. Early-eluting RLU peak fractions contained HiBiT VLPs and were stored at 4°C. To preserve stored HiBiT VLPs, sodium azide was added at a final concentration of 0.02%. SARS-CoV-2 structural proteins were identified in the VLP preparations by Western immunoblotting, as described in (*19*).

Production and isolation of tEVs

HEK293T cells were LipoD293 transfected with 16 μg of pcDNA3.1-hACE2-LgBiT per 145-cm^2 plate (for hACE2-LgBiT tEVs) or with 8 μg of pcDNA3/1-hACE2-C9 and 8 μg of pCAGGS-S15-LgBiT (for hACE2 + LgBiT tEVs). Transfected cells were incubated from 16 to 48 hours p.t. in SFM, with tEV-containing media, and then harvested, clarified, and concentrated >160-fold, according to VLP isolation procedures. SEC purification was also carried out as per VLP isolation protocols, but with HiBiT-N replacing LgBiT for detection of the early-eluting tEV peak fractions. Purified tEVs were stored at 4°C in PBS (pH 7.4) with 0.02% sodium azide preservative.

VLP-tEV fusion assay

Concentrated VLPs were mixed with SEC-purified tEVs in 96-well white-walled plates and then diluted to 40 μl per well with PBS containing Nano-Glo HiBiT Extracellular Detection substrate (Promega). Monomeric and dimeric SARS-CoV-2 inhibitory peptides were then added, and after 15 min at 4°C, 6- (1-tosylamido-2-phenyl) ethyl chloromethyl ketone (TPCK)-trypsin (Sigma-Aldrich) was added to a final concentrations of 50 ng/μl or titrated to the indicated final concentrations. Inhibitory peptides were evaluated throughout a 0-to-1 μM concentration range. Plates were placed into a 37°C prewarmed stage, and relative luminescence units (RLUs) were read at 2-min intervals. Fusion levels, measured as RLUs above spikeless VLP background levels, were calculated and plotted at indicated time point(s) after shift to 37°C.

Chemicals and peptides

The peptide ($SARS_{HRC}$) corresponding to residues 1168 to 1203 of SARS-CoV-2 S with a C-terminal -GSGSGC spacer sequence was prepared by solid-phase peptide synthesis. The $SARS_{HRC}$ peptide was acetylated at the N terminus and amidated at the C terminus. The crude peptide was purified by reverse-phase high-performance liquid chromatography (HPLC) and characterized by matrix-assisted laser desorption ionization–time-of-flight mass spectrometry. $[SARS_{HRC}]_2$-PEG_{11} (dimeric peptide without lipid) and $[SARS_{HRC}$-$PEG_4]_2$-chol were synthesized via chemoselective Thiol-Michael addition reactions between the terminal thiol group on the peptide cysteine residue and maleimide functional polyethylene glycol (PEG) linkers or PEG-cholesterol linkers as previously described (*5*). Purification by HPLC and lyophilization yielded the peptide-lipid conjugates as white powders. $[SARS_{HRC}]_2$-PEG_{11} or $[SARS_{HRC}$-$PEG_4]_2$-chol was dissolved in Dulbecco's phosphate-buffered saline to a concentration of 10 μM before use.

Cryo-ET preparation

Lacey carbon gold grids, containing a continuous layer of thin carbon (Ted Pella), were plasma cleaned with Fischione M1070 Nanoclean on 70% power for 20 s with a 25% oxygen and 75% argon gas mixture. Samples containing a combination of 1:4 VLP-to-tEV ratio, in the presence or absence of trypsin (250 ng/μl), and/or 250 nM $[SARS_{HRC}]_2$-PEG_{11} or $[SARS_{HRC}$-$PEG_4]_2$-chol were incubated for 30 min either at 37° or 4°C. To aid in tomogram fiducial alignment, 5-nm gold nanoparticles at 1.0 optical density (O.D.) concentration in citrate buffer (Sigma-Aldrich) were added to each sample as 10% of the final concentration. After the incubation period, 6 μl of each sample was applied to the Lacey carbon gold grids, incubated for 10 s in 100% humidity at 4°C, blotted, and plunge frozen in liquid ethane using a Vitrobot (Mark IV; Thermo Fisher Scientific Co.).

Cryo-ET data collection

For Figs. 2 (B, C, and E), 3 (B to M), 4 (B to E and J), and 5 and figs. S4, S5, and S8, the vitrified grids were imaged with a Titan Krios

300-kV transmission electron microscope (Thermo Fisher Scientific Co.) equipped with a direct detection Gatan K3 camera and an energy filter slit width of 20 eV. Images were captured at a magnification of 53,000 kX and later binned by a factor of 4, giving a pixel size of 6.48 Å per pixel at the specimen level. Images were acquired with SerialEM software with a 5- to 8-μm defocus and a dose symmetric tilt series at 3° steps from 54° to −54° with a total dose of ~100 e−/Å^2.

For Figs. 2D and 4 (H and I) and figs. S3, S6, and S7, the vitrified grids were imaged with the Titan Halo 300 kV transmission electron microscope (Thermo Fisher Scientific Co.), equipped with a direct detection Gatan K3 camera without an energy filter and a Gatan 626 side-entry cryo-holder. Images were captured at a magnification of 22,500 kX and later binned by a factor of 4, giving a pixel size of either 5.44 Å per pixel (fig. S3) or 5.22 Å per pixel (Figs. 2D and 4, H and I, and figs. S6 and S7) at the specimen level. Images were acquired with SerialEM software (*29*) with a 4- to 7-μm defocus and a bidirectional tilt series starting at −9° moving in 3° steps to 51° and then returning back to −9° to −51° with a total dose of ~100 e−/Å^2.

Cryo-ET data processing

All micrograph frames were aligned and motion corrected using WarpEM (*30*). Tomograms were reconstructed using IMOD ETomo (*31*) with fiducial markers. All reconstructed tomograms were visualized using ImageJ, IMOD (*31*), and Chimera (*32*). Measurements of VLP (n = 50) and tEV (n = 50) diameters and the membrane-membrane spike distances (n = 192) were performed using the plot profile function, using the half-maximal density between two membranes. Distance measurements in Fig. 4 (F and G) were obtained in ImageJ, using the plot profile function with a line width of 4 Å. Distances were exported into Excel, and averages were obtained. Isosurface representations were made in Chimera. PDB structures in Figs. 2 (B and C), 3E, and 5 (D and G) and figs. S5 (D, H, and L) were fitted into the density maps using Chimera's Fit in Map function.

Subtomogram averaging of hACE2

The ab initio hACE2 subtomogram averaging process was performed using the Dynamo software package (*33*, *34*) on six tomograms with VLPs containing spikes interacting with tEVs (including tomograms in Figs. 3B, 4D, and 5, E and N). Subvolumes of the tEV surfaces containing hACE2 $(415)^3$ Å were extracted from 2× binned tomograms. The first round of alignment with a 360° azimuth range was followed by centering on a dimeric hACE2 density and recropping to $(311)^3$ Å. This was followed by a second round of refinement with a 120° azimuth range on the centered particles. The resulting subvolumes were classified into five classes by principal components analysis in the Dynamo software package. Two classes contained the dimeric hACE2 and were combined for further subtomogram averaging. Subvolumes in rounds 3 to 5 (18 iterations) of these combined classes were aligned with decreasing the azimuth range to 40° in the presence of cylindrical mask encompassing only the hACE2 density. Overlapping particles with less than 30 Å of separation were removed at the end of the third round. The final subtomogram average resulted in a calculated resolution of 19 Å at 0.143-Å cutoff value. Resolution for the resulting maps was estimated by Fourier shell correlation with a 0.143-Å cutoff value using 3DFSC (*35*). Model fitting of hACE2 was performed in ChimeraX (*36*, *37*) using the cryo-EM structure of ACE2 (PDB ID: 6M1D) (*11*).

Modeling SARS-CoV-2 S protein–mediated fusion

Molecular modeling and steered simulations were carried out as described by de Vries *et al.* (*5*). Briefly, Molecular Maya (https://clarafi.com/tools/mmaya/) was used to model and simulate the inhibitory lipopeptide, the full-length SARS-CoV 2 Spike (S) prefusion, and prehairpin and postfusion structures, using a combination of molecular mechanics force fields including MMFF94 (*38*), CHARMM C36 (*39*), and Martini (*40*). Simulations were run using Autodesk Maya's nucleus solver, and additional restraints native to the nucleus solver (nConstraints) were used to stabilize the molecules during interactive steering. To model the intermediates of the S protein, simulations were run to progressively steer the HRN region (residues 910 to 985) toward the aligned postfusion structure using distances obtained from tomograms, leading to the extension of the CH coiled coil by HRN. The remaining regions of the model were restrained with elastic networks or position restraints to preserve local secondary structure.

SUPPLEMENTARY MATERIALS

Supplementary material for this article is available at https://science.org/doi/10.1126/sciadv.abo3153

View/request a protocol for this paper from *Bio-protocol*.

REFERENCES AND NOTES

1. A. C. Walls, Y.-J. Park, M. A. Tortorici, A. Wall, A. T. McGuire, D. Veesler, Structure, function, and antigenicity of the SARS-CoV-2 spike glycoprotein. *Cell* **181**, 281–292.e6 (2020).
2. E. Qing, T. Kicmal, B. Kumar, G. M. Hawkins, E. Timm, S. Perlman, T. Gallagher, Dynamics of SARS-CoV-2 spike proteins in cell entry: Control elements in the amino-terminal domains. *MBio* **12**, e01590 (2021).
3. V. K. Outlaw, F. T. Bovier, M. C. Mears, M. N. Cajimat, Y. Zhu, M. J. Lin, A. Addetia, N. A. P. Lieberman, V. Peddu, X. Xie, P. Y. Shi, A. L. Greninger, S. H. Gellman, D. A. Bente, A. Moscona, M. Porotto, Inhibition of coronavirus entry in vitro and ex vivo by a lipid-conjugated peptide derived from the SARS-CoV-2 spike glycoprotein HRC domain. *MBio* **11**, e01935-20 (2020).
4. B. J. Bosch, R. van der Zee, C. A. de Haan, P. J. Rottier, The coronavirus spike protein is a class I virus fusion protein: Structural and functional characterization of the fusion core complex. *J. Virol.* **77**, 8801–8811 (2003).
5. R. D. de Vries, K. S. Schmitz, F. T. Bovier, C. Predella, J. Khao, D. Noack, B. L. Haagmans, S. Herfst, K. N. Stearns, J. Drew-Bear, S. Biswas, B. Rockx, G. McGill, N. V. Dorrello, S. H. Gellman, C. A. Alabi, R. L. de Swart, A. Moscona, M. Porotto, Intranasal fusion inhibitory lipopeptide prevents direct-contact SARS-CoV-2 transmission in ferrets. *Science* **371**, 1379–1382 (2021).
6. S. Xia, M. Liu, C. Wang, W. Xu, Q. Lan, S. Feng, F. Qi, L. Bao, L. du, S. Liu, C. Qin, F. Sun, Z. Shi, Y. Zhu, S. Jiang, L. Lu, Inhibition of SARS-CoV-2 (previously 2019-nCoV) infection by a highly potent pan-coronavirus fusion inhibitor targeting its spike protein that harbors a high capacity to mediate membrane fusion. *Cell Res.* **30**, 343–355 (2020).
7. J. Lan, J. Ge, J. Yu, S. Shan, H. Zhou, S. Fan, Q. Zhang, X. Shi, Q. Wang, L. Zhang, X. Wang, Structure of the SARS-CoV-2 spike receptor-binding domain bound to the ACE2 receptor. *Nature* **581**, 215–220 (2020).
8. J. Shang, G. Ye, K. Shi, Y. Wan, C. Luo, H. Aihara, Q. Geng, A. Auerbach, F. Li, Structural basis of receptor recognition by SARS-CoV-2. *Nature* **581**, 221–224 (2020).
9. D. Wrapp, N. Wang, K. S. Corbett, J. A. Goldsmith, C. L. Hsieh, O. Abiona, B. S. Graham, J. S. McLellan, Cryo-EM structure of the 2019-nCoV spike in the prefusion conformation. *Science* **367**, 1260–1263 (2020).
10. C. Liu, L. Mendonça, Y. Yang, Y. Gao, C. Shen, J. Liu, T. Ni, B. Ju, C. Liu, X. Tang, J. Wei, X. Ma, Y. Zhu, W. Liu, S. Xu, Y. Liu, J. Yuan, J. Wu, Z. Liu, Z. Zhang, L. Liu, P. Wang, P. Zhang, The architecture of inactivated SARS-CoV-2 with postfusion spikes revealed by Cryo-EM and Cryo-ET. *Structure* **28**, 1218–1224.e4 (2020).
11. R. Yan, Y. Zhang, Y. Li, L. Xia, Y. Guo, Q. Zhou, Structural basis for the recognition of the SARS-CoV-2 by full-length human ACE2. *Science* **367**, 1444–1448 (2020).
12. Z. Ke, J. Oton, K. Qu, M. Cortese, V. Zila, L. McKeane, T. Nakane, J. Zivanov, C. J. Neufeldt, B. Cerikan, J. M. Lu, J. Peukes, X. Xiong, H. G. Kräusslich, S. H. W. Scheres, R. Bartenschlager, J. A. G. Briggs, Structures and distributions of SARS-CoV-2 spike proteins on intact virions. *Nature* **588**, 498–502 (2020).
13. S. Klein, M. Cortese, S. L. Winter, M. Wachsmuth-Melm, C. J. Neufeldt, B. Cerikan, M. L. Stanifer, S. Boulant, R. Bartenschlager, P. Chlanda, SARS-CoV-2 structure

and replication characterized by in situ cryo-electron tomography. *Nat. Commun.* **11**, 5885 (2020).
14. G. Wolff, R. W. A. L. Limpens, J. C. Zevenhoven-Dobbe, U. Laugks, S. Zheng, A. W. M. de Jong, R. I. Koning, D. A. Agard, K. Grünewald, A. J. Koster, E. J. Snijder, M. Bárcena, A molecular pore spans the double membrane of the coronavirus replication organelle. *Science* **369**, 1395–1398 (2020).
15. Y. H. Kim, J. E. Donald, G. Grigoryan, G. P. Leser, A. Y. Fadeev, R. A. Lamb, W. F. DeGrado, Capture and imaging of a prehairpin fusion intermediate of the paramyxovirus PIV5. *Proc. Natl. Acad. Sci. U.S.A.* **108**, 20992–20997 (2011).
16. D. J. Benton, S. J. Gamblin, P. B. Rosenthal, J. J. Skehel, Structural transitions in influenza haemagglutinin at membrane fusion pH. *Nature* **583**, 150–153 (2020).
17. M. S. Ladinsky, P. N. P. Gnanapragasam, Z. Yang, A. P. West, M. S. Kay, P. J. Bjorkman, Electron tomography visualization of HIV-1 fusion with target cells using fusion inhibitors to trap the pre-hairpin intermediate. *eLife* **9**, e58411 (2020).
18. T. C. Marcink, T. Wang, A. des Georges, M. Porotto, A. Moscona, Human parainfluenza virus fusion complex glycoproteins imaged in action on authentic viral surfaces. *PLOS Pathog.* **16**, e1008883 (2020).
19. B. Kumar, G. M. Hawkins, T. Kicmal, E. Qing, E. Timm, T. Gallagher, Assembly and entry of severe acute respiratory syndrome coronavirus 2 (SARS-CoV2): Evaluation using virus-like particles. *Cell* **10**, 853 (2021).
20. B. Turoňová, M. Sikora, C. Schürmann, W. J. H. Hagen, S. Welsch, F. E. C. Blanc, S. von Bülow, M. Gecht, K. Bagola, C. Hörner, G. van Zandbergen, J. Landry, N. T. D. de Azevedo, S. Mosalaganti, A. Schwarz, R. Covino, M. D. Mühlebach, G. Hummer, J. K. Locker, M. Beck, In situ structural analysis of SARS-CoV-2 spike reveals flexibility mediated by three hinges. *Science* **370**, 203–208 (2020).
21. A. B. Vogel, I. Kanevsky, Y. Che, K. A. Swanson, A. Muik, M. Vormehr, L. M. Kranz, K. C. Walzer, S. Hein, A. Güler, J. Loschko, M. S. Maddur, A. Ota-Setlik, K. Tompkins, J. Cole, B. G. Lui, T. Ziegenhals, A. Plaschke, D. Eisel, S. C. Dany, S. Fesser, S. Erbar, F. Bates, D. Schneider, B. Jesionek, B. Sänger, A. K. Wallisch, Y. Feuchter, H. Junginger, S. A. Krumm, A. P. Heinen, P. Adams-Quack, J. Schlereth, S. Schille, C. Kröner, R. de la C. G. Garcia, T. Hiller, L. Fischer, R. S. Sellers, S. Choudhary, O. Gonzalez, F. Vascotto, M. R. Gutman, J. A. Fontenot, S. Hall-Ursone, K. Brasky, M. C. Griffor, S. Han, A. A. H. Su, J. A. Lees, N. L. Nedoma, E. H. Mashalidis, P. V. Sahasrabudhe, C. Y. Tan, D. Pavliakova, G. Singh, C. Fontes-Garfias, M. Pride, I. L. Scully, T. Ciolino, J. Obregon, M. Gazi, R. Carrion Jr., K. J. Alfson, W. V. Kalina, D. Kaushal, P. Y. Shi, T. Klamp, C. Rosenbaum, A. N. Kuhn, Ö. Türeci, P. R. Dormitzer, K. U. Jansen, U. Sahin, BNT162b vaccines protect rhesus macaques from SARS-CoV-2. *Nature* **592**, 283–289 (2021).
22. R. Henderson, R. J. Edwards, K. Mansouri, K. Janowska, V. Stalls, S. M. C. Gobeil, M. Kopp, D. Li, R. Parks, A. L. Hsu, M. J. Borgnia, B. F. Haynes, P. Acharya, Controlling the SARS-CoV-2 spike glycoprotein conformation. *Nat. Struct. Mol. Biol.* **27**, 925–933 (2020).
23. X. Fan, D. Cao, L. Kong, X. Zhang, Cryo-EM analysis of the post-fusion structure of the SARS-CoV spike glycoprotein. *Nat. Commun.* **11**, 3618 (2020).
24. H. E. Park, J. A. Gruenke, J. M. White, Leash in the groove mechanism of membrane fusion. *Nat. Struct. Biol.* **10**, 1048–1053 (2003).
25. L. J. Calder, P. B. Rosenthal, Cryomicroscopy provides structural snapshots of influenza virus membrane fusion. *Nat. Struct. Mol. Biol.* **23**, 853–858 (2016).
26. C. B. Plescia, E. A. David, D. Patra, R. Sengupta, S. Amiar, Y. Su, R. V. Stahelin, SARS-CoV-2 viral budding and entry can be modeled using BSL-2 level virus-like particles. *J. Biol. Chem.* **296**, 100103 (2021).
27. M. Kielian, Mechanisms of virus membrane fusion proteins. *Annu. Rev. Virol.* **1**, 171–189 (2014).
28. D. Pinto, M. M. Sauer, N. Czudnochowski, J. S. Low, M. A. Tortorici, M. P. Housley, J. Noack, A. C. Walls, J. E. Bowen, B. Guarino, L. E. Rosen, J. di Iulio, J. Jerak, H. Kaiser, S. Islam, S. Jaconi, N. Sprugasci, K. Culap, R. Abdelnabi, C. Foo, L. Coelmont, I. Bartha, S. Bianchi, C. Silacci-Fregni, J. Bassi, R. Marzi, E. Vetti, A. Cassotta, A. Ceschi, P. Ferrari, P. E. Cippà, O. Giannini, S. Ceruti, C. Garzoni, A. Riva, F. Benigni, E. Cameroni, L. Piccoli, M. S. Pizzuto, M. Smithey, D. Hong, A. Telenti, F. A. Lempp, J. Neyts, C. Havenar-Daughton, A. Lanzavecchia, F. Sallusto, G. Snell, H. W. Virgin, M. Beltramello, D. Corti, D. Veesler, Broad betacoronavirus neutralization by a stem helix–specific human antibody. *Science* **373**, 1109–1116 (2021).
29. D. N. Mastronarde, Automated electron microscope tomography using robust prediction of specimen movements. *J. Struct. Biol.* **152**, 36–51 (2005).
30. X. Li, P. Mooney, S. Zheng, C. R. Booth, M. B. Braunfeld, S. Gubbens, D. A. Agard, Y. Cheng, Electron counting and beam-induced motion correction enable near-atomic-resolution single-particle cryo-EM. *Nat. Methods* **10**, 584–590 (2013).
31. J. R. Kremer, D. N. Mastronarde, J. R. McIntosh, Computer visualization of three-dimensional image data using IMOD. *J. Struct. Biol.* **116**, 71–76 (1996).
32. E. F. Pettersen, T. D. Goddard, C. C. Huang, G. S. Couch, D. M. Greenblatt, E. C. Meng, T. E. Ferrin, UCSF Chimera—A visualization system for exploratory research and analysis. *J. Comput. Chem.* **25**, 1605–1612 (2004).
33. D. Castano-Diez, M. Kudryashev, H. Stahlberg, Dynamo catalogue: Geometrical tools and data management for particle picking in subtomogram averaging of cryo-electron tomograms. *J. Struct. Biol.* **197**, 135–144 (2017).
34. D. Castano-Diez, M. Kudryashev, M. Arheit, H. Stahlberg, Dynamo: A flexible, user-friendly development tool for subtomogram averaging of cryo-EM data in high-performance computing environments. *J. Struct. Biol.* **178**, 139–151 (2012).
35. Y. Z. Tan, P. R. Baldwin, J. H. Davis, J. R. Williamson, C. S. Potter, B. Carragher, D. Lyumkis, Addressing preferred specimen orientation in single-particle cryo-EM through tilting. *Nat. Methods* **14**, 793–796 (2017).
36. T. D. Goddard, C. C. Huang, E. C. Meng, E. F. Pettersen, G. S. Couch, J. H. Morris, T. E. Ferrin, UCSF ChimeraX: Meeting modern challenges in visualization and analysis. *Protein Sci.* **27**, 14–25 (2018).
37. E. F. Pettersen, T. D. Goddard, C. C. Huang, E. C. Meng, G. S. Couch, T. I. Croll, J. H. Morris, T. E. Ferrin, UCSF ChimeraX: Structure visualization for researchers, educators, and developers. *Protein Sci.* **30**, 70–82 (2021).
38. R. B. Best, X. Zhu, J. Shim, P. E. M. Lopes, J. Mittal, M. Feig, A. D. MacKerell Jr., Optimization of the additive CHARMM all-atom protein force field targeting improved sampling of the backbone ϕ, ψ and side-chain $\chi1$ and $\chi2$ dihedral angles. *J. Chem. Theory Comput.* **8**, 3257–3273 (2012).
39. S. J. Marrink, H. J. Risselada, S. Yefimov, D. P. Tieleman, A. H. de Vries, The MARTINI force field: Coarse grained model for biomolecular simulations. *J. Phys. Chem. B* **111**, 7812–7824 (2007).
40. Y. Cai, J. Zhang, T. Xiao, H. Peng, S. M. Sterling, R. M. Walsh Jr., S. Rawson, S. Rits-Volloch, B. Chen, Distinct conformational states of SARS-CoV-2 spike protein. *Science* **369**, 1586–1592 (2020).

Acknowledgments

Funding: This work was supported by funding from the National Institutes of Health (AI152275 to T.C.M.; AI060699 to T.G.; AI121349 and AI160953 to M.P.; GM133598 to A.d.G.; and AI114736 and AI160961 to A.M.) and by the Sharon Golub Fund at Columbia University Vagelos College of Physicians and Surgeons. **Author contributions:** conceptualization: T.C.M., T.G., M.P., and A.M.; formal analysis: T.C.M., T.G., M.P., A.d.G., and A.M.; funding acquisition: T.C.M., M.P., T.G., A.d.G., and A.M.; investigation: T.C.M., T.K., E.A., Z.Z., G.Z., K.L.G., M.I., and J.D.-B.; resources: A.d.G., M.P., and A.M.; supervision: T.G., M.P., A.d.G., and A.M.; visualization: T.C.M., J.K., G.M., M.P., and A.M.; writing—original draft: T.C.M. and A.M.; final version: all coauthors provided feedback to the final draft. **Competing interests:** A.M. and M.P. are inventors on patent applications related to this work as follows: WO/2021/216891, published 28 October 2021, filed 22 April 2021, by The Trustees of Columbia University in the City of New York and Wisconsin Alumni Research Foundation; and WO/2022/081711, published 21 April 2022, filed 13 October 2021, by The Trustees of Columbia University in the City of New York, Erasmus University Medical Center, and INSERM. A.M. and M.P. expect to have future financial interests in Thylacine Bio, a company developing antiviral peptides. The authors declare that they have no other competing interests. **Data and materials availability:** Original tomograms have been deposited in the Electron Microscopy Data Bank (EMDB) with the following accession codes: EMD-24599 for Figs. 4J and 5 (N and O) and movie S3; EMD-24600 for Fig. 5 (L and M) and movie S2; EMD-24601 for Fig. 3 (B to E) and movie S1; EMD-24602 for Fig. 5 (E to G); EMD-24603 for Fig. 4 (D and E); and EMD-24604 for Fig. 3 (H to J). The final subtomogram averaged density of hACE2 has been deposited in the EMDB with the accession code EMD-26679. Prealigned tilt series for all tomograms have been deposited in the Electron Microscopy Public Image Archive (EMPIAR) database with the accession code EMPIAR-10788. All other relevant data needed to evaluate the conclusions in the paper are present in the paper and/or the Supplementary Materials. The $[SARS_{HRC}]_2$-PEG_{11} or $[SARS_{HRC}$- $PEG_4]_2$-chol peptides can be provided by the Trustees of Columbia University, NYC, pending scientific review and a completed material transfer agreement. Requests for the $[SARS_{HRC}]_2$-PEG_{11} or $[SARS_{HRC}$- $PEG_4]_2$-chol peptides should be submitted to the corresponding authors under a material agreement with Columbia University.

Submitted 28 January 2022
Accepted 7 July 2022
Published 19 August 2022
10.1126/sciadv.abo3153